

Ships and Offshore Structures

ISSN: 1744-5302 (Print) 1754-212X (Online) Journal homepage: www.tandfonline.com/journals/tsos20

Robust stabilization of a three-axis ship-mounted mobile antenna system

İbrahim Sina Kuseyri

To cite this article: İbrahim Sina Kuseyri (07 Jul 2026): Robust stabilization of a three-axis ship-mounted mobile antenna system, Ships and Offshore Structures, DOI: 10.1080/17445302.2026.2697035

To link to this article: https://doi.org/10.1080/17445302.2026.2697035

Published online: 07 Jul 2026.

Submit your article to this journal

View related articles

View Crossmark data

Full Terms & Conditions of access and use can be found at
https://www.tandfonline.com/action/journalInformation?journalCode=tsos20

SHIPS AND OFFSHORE STRUCTURES
https://doi.org/10.1080/17445302.2026.2697035

Taylor & Francis
by informa

Check for updates

Robust stabilization of a three-axis ship-mounted mobile antenna system

İbrahim Sina Kuseyri

Mechanical Engineering Department, Marmara University, İstanbul, Türkiye

ABSTRACT

The demand for on-line information in diverse environments has driven the development of mobile satellite communication terminals. These high-data-rate systems require antenna pointing accuracy within fractions of a degree. In mobile applications, however, platform base motion complicates the pointing task and must be compensated. To mitigate these disturbances and ensure uninterrupted communication, gimbaled motorized pedestals are employed. This paper investigates the robust stability and performance of a three-axis ship-mounted mobile antenna stabilization system. The azimuth axis was selected for detailed analysis, as it is most affected by dynamic coupling. Typical uncertainties in the system dynamics were defined, and an H_∞ controller was synthesized for the closed-loop uncertain system. The controller was benchmarked against a baseline PI controller, and the margins of robust stability and performance were computed. The analysis pinpointed the dominant uncertainty sources that undermine system robustness, forming the basis for targeted controller improvements.

ARTICLE HISTORY
Received 15 December 2025
Accepted 24 June 2026

KEYWORDS
Mobile antenna; robust stabilization; three-axis gimbal control; μ-analysis

1. Introduction

In the age of pervasive information technology, mobile data communication plays a pivotal role in delivering broadband connectivity across the globe. Satellite constellations ensure that it is always possible to establish a link with a satellite, regardless of the antenna's position on Earth. However, this connectivity relies not only on satellite availability but also on the precise tracking and stabilization of the antenna system – especially when mounted on dynamic, non-stationary platforms like ships, vehicles, or aircraft. When a ship-mounted antenna, for example, locks onto a satellite, the vessel's pitch, roll, and yaw – primarily due to wave activity – can disrupt the line of sight, thereby degrading or completely severing the communication link. To mitigate these effects, servo-mechanical pedestal systems equipped with automatic control mechanisms are used. These systems consist of a gimbal structure – allowing rotational motion – combined with motors, gyroscopes, bearings, and payload interfaces. They function to dynamically adjust the mechanical posture of the antenna, isolating it from disturbances and preserving its pointing direction. This ensures continuous, global satellite communication, even when the carrier is in motion.

In practice, antenna pedestals come in two-axis and three-axis configurations. The common azimuth – elevation two-axis pedestal is often preferred due to its lower cost, compactness, and inherent stiffness. Its hemispheric coverage from the horizon to zenith makes it suitable for a wide range of applications. However, this configuration suffers from a critical limitation – gimbal lock – which occurs when the elevation gimbal is positioned at 90°, causing the line of sight to align with the azimuth axis and effectively reducing the system to a single degree of freedom. To resolve this, a third axis – known as the cross-level (x-level) axis – is introduced as depicted in Figure 1, forming an azimuth – x-level – elevation configuration. This additional degree of freedom enables the system to maintain maneuverability even in the 'keyhole' region where gimbal lock occurs. Tilting the x-level axis between 30° and 35° improves structural stiffness without significantly compromising performance.

Compared to fixed-base manipulators or rotating simulators, modeling mobile antenna systems is more challenging. For example, Love et al. (2004) studied the influence of wave disturbances on a ship-mounted manipulator using a Lagrangian framework, but a complete dynamic derivation was not pursued. High-precision tracking requires a unified model that captures all subsystems and couplings. Kuseyri (2017a) derived the equations of motion for a three-axis ship-mounted antenna system using the Newton–Euler approach.

CONTACT İbrahim Sina Kuseyri sina.kuseyri@marmara.edu.tr

© 2026 Informa UK Limited, trading as Taylor & Francis Group

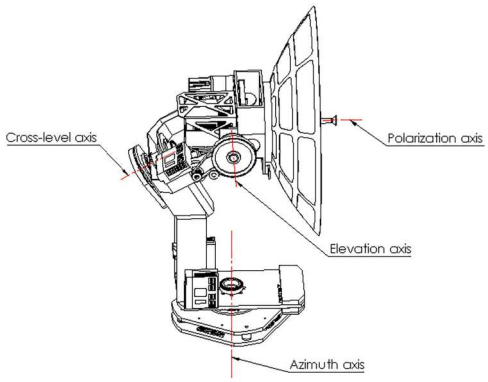

Figure 1. Three-axis antenna pedestal system (Kuseyri 2017a).

Most feedback control system designs aim to satisfy the requirements of a nominal model. While such designs may be adequate for the nominal case, they often become insufficient when the actual system parameters deviate from the nominal values. Sources of uncertainty include inertia variation, gear ratios, stiffness, friction, backlash, and actuator saturation. These parameters are not constant; they change with elevation angle, temperature, lubrication conditions, and mechanical wear. In antenna systems, the dynamic model is particularly difficult to obtain because of nonlinearities and high-order elastic effects. Although parameters such as inertia, gear ratios, stiffness, friction, and actuator limits are usually provided by manufacturers or estimated experimentally, these values are approximate and vary during operation. For example, the inertia experienced by the azimuth axis strongly depends on the antenna's elevation angle, with higher elevations generally reducing the effective inertia. Similarly, friction characteristics vary with temperature, lubrication quality, and long-term wear. Such parametric and dynamic fluctuations introduce uncertainty into the antenna model, which must be quantified over the relevant frequency band to establish meaningful uncertainty bounds. To improve command-following and disturbance-rejection performance in the presence of these nonlinearities and uncertainties, robust control techniques become necessary.

In this context, Kim et al. (2010) developed a dynamic model for the stabilization loop of a two-axis gimbaled sensor system and identified system parameters through practical experiments. They designed an H_∞ controller that combined model matching with the mixed-sensitivity approach to enhance command-following and disturbance-rejection performance under external disturbances and model uncertainties. Hong and Cho (2012) experimentally estimated the parameters of the dynamic equations of a two-axis tracking radar stabilization system by minimizing prediction error. They subsequently designed mixed-sensitivity H_∞ robust controllers to address the conflicting requirements of robustness and performance in the presence of uncertainties. Ren et al. (2019) proposed a disturbance compensation strategy based on disturbance observer control (DOBC). They formulated uncertainties, friction, and coupling deficiencies of the gimbal system as a disturbance-suppression problem and adopted an H_∞-based filter design to ensure robust stability. Safa and Abdolmalaki (2019) developed state-feedback and output-feedback controllers for two-axis stabilization platforms considering dynamic mass imbalance. Their derivation assumed that all system modeling parameters were unknown but bounded. Baskın and Leblebicioğlu (2017) presented robust controller designs within the LQG/LTR, H_∞, and μ-synthesis frameworks for a two-axis gimbal stabilization platform, comparing their robust stability and performance characteristics. Kuseyri (2017b) designed a centralized MIMO H_∞ robust controller for a three-axis ship-mounted stabilization platform and demonstrated superior stabilization performance compared to decentralized, single-axis PI-based control. Nguyen and Nguyen (2019) introduced a two-degree-of-freedom robust controller for the stabilization loop of a two-axis gimbal system. Their structure was shown to guarantee both disturbance rejection and reference tracking simultaneously. Lee et al. (2020) designed a dual active controller consisting of an inner compensator and a feedback controller within the H_∞ framework. A comparative experimental study was conducted between the designed controller and an integral sliding-mode controller (ISMC). Hajjem et al. (2022) proposed a robust control strategy for two-axis tracking antennas using fractional-order robust controllers and demonstrated superior performance compared to conventional PID control. Şahin (2024) developed a fuzzy-logic-based self-tuning PID controller for two-axis gimbal stabilization system to improve robustness. Beyond the linear robust-control literature surveyed above, recent work has explored observer-based and nonlinear approaches to gimbal stabilization. Disturbance-observer-based control (DObC) estimates lumped uncertainties from measurable signals and cancels their effect through feedback (Sariyildiz et al. 2020). Composite architectures combining disturbance observers with sliding-mode or super-twisting outer loops have been applied to optoelectronic gimbals (Wang et al. 2018) and to spacecraft attitude and orbit – attitude – vibration stabilization (Lyu et al. 2022, 2026), with the latter using a nonfragile observer formulation that tolerates gain perturbation under an LMI convergence condition – a property of practical interest for fixed-point gimbal hardware.

These observer-based architectures can outperform single-loop H_∞ designs when disturbance content is dominantly low- and mid-frequency. Nonlinear schemes such as sliding-mode (Lee et al. 2020) and fractional-order (Hajjem et al. 2022) controllers have also been reported for two-axis gimbals, and fuzzy-logic-based self-tuning PID (Şahin 2024) has been used to adapt loop gains to plant variability.

The present paper does not propose a new controller within these families; rather, it provides the diagnostic step that must precede their adoption, namely an explicit, frequency-domain attribution of robustness loss to each individual uncertainty source. Using a signal-based H_∞ synthesis approach, we explicitly characterize each uncertainty that affects the system dynamics in the frequency domain. We then analyze the system's robust stability and performance to quantify the individual impact of each uncertainty source. This enables targeted robustness improvements by focusing on the dominant contributors to stability and performance degradation. To the best of our knowledge, the effects of specific uncertainties on robust stability and robust performance have not previously been quantified for gimbal-based stabilization systems. Rather than H_∞ synthesis in isolation (Kim et al. 2010; Hong and Cho 2012; Baskın and Leblebicioğlu 2017; Kuseyri 2017b; Nguyen and Nguyen 2019), the contribution of this paper is a structured-uncertainty framework combining several elements in a single reproducible analysis. The azimuth-axis closed loop is represented through an explicit LFT model with four physically interpretable structured-uncertainty blocks – backlash, inertia variation, friction, and torsional flexibility – each defined through dedicated weighting filters W_b, W_J, W_f, W_h, in contrast to published gimbal-control studies that typically lump uncertainties into a single multiplicative block. On this basis, the synthesized H_∞ controller is benchmarked side by side against a PI baseline tuned for the same disturbance band, with nominal performance, the μ-based robust stability margin, and the robust performance margin all reported under identical uncertainty specifications. A frequency-by-frequency μ-decomposition then attributes the loss of robust stability and robust performance to individual blocks through per-block substitution (one block 'hot', others nominal) and a 25%-uplift sensitivity bar chart at the critical frequency. This analysis identifies friction and backlash as the dominant constraints on both margins and prioritizes remediation paths – inner torque loop, model-based friction compensation, backlash inversion/governors, μ-synthesis, disturbance observers – by their relevance to the dominant blocks.

The structure of the paper is as follows. Section 2 formulates the linear dynamic model of the antenna pedestal system. Section 3 develops a benchmark PI controller and an H_∞ controller for the uncertain system and specifies the robust stability and performance requirements. Section 4 reports numerical simulations evaluating the stability and performance of the synthesized H_∞ controller. Section 5 examines the results and provides concluding remarks.

2. Antenna gimbal model

The ship-mounted three-axis antenna pedestal analyzed in this paper is illustrated in Figure 2. It consists of three subsystems arranged from the outermost to the innermost: the azimuth subsystem (A), the cross-level subsystem (L), and the elevation subsystem (E). The antenna responsible for transmitting and receiving satellite signals is mounted on the elevation subsystem. Each subsystem is driven by its servomotor to compensate for hull motion disturbances, thereby maintaining accurate antenna pointing toward the designated satellite.

The angular velocities are defined in the body, azimuth, cross-level, and elevation reference frames, respectively, as follows (Kuseyri 2017a).

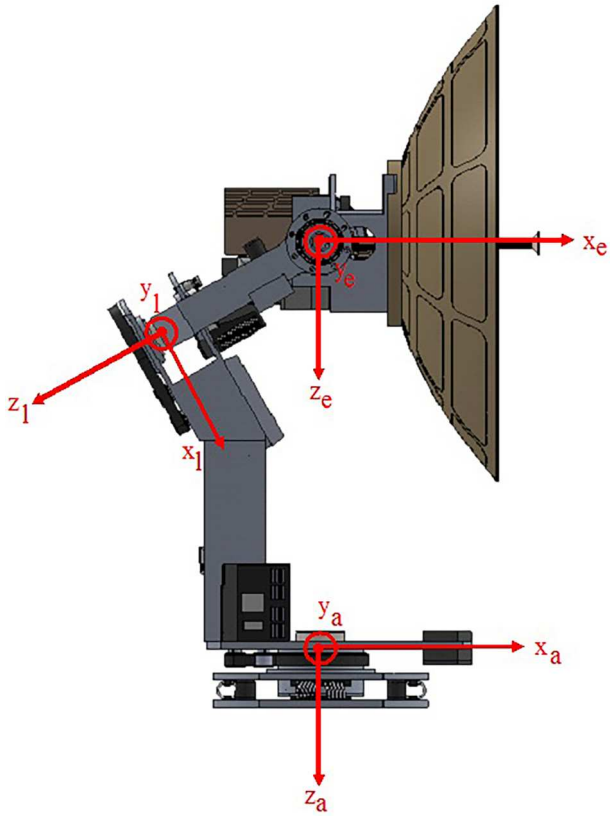

Figure 2. Antenna pedestal and reference frames attached (Kuseyri 2017a).

$\omega_B := (p_b\, q_b\, r_b)^{\mathrm{T}}$, $\omega_A := (p_a\, q_a\, r_a)^{\mathrm{T}}$, $\omega_L := (p_l\, q_l\, r_l)^{\mathrm{T}}$, and $\omega_E := (p_e\, q_e\, r_e)^{\mathrm{T}}$. Using 3-2-1 Euler angles

$$\omega_B = \begin{pmatrix} \dot{\phi} - \dot{\psi}\sin\theta \\ \dot{\theta}\cos\phi + \dot{\psi}\cos\theta\sin\phi \\ \dot{\psi}\cos\theta\cos\phi - \dot{\theta}\sin\phi \end{pmatrix}. \tag{1}$$

Angular velocities in other frames follow from kinematics and control-axis rates:

$$\omega_A = R_B^A\omega_B + \begin{pmatrix} 0 \\ 0 \\ \dot{\nu}_1 \end{pmatrix}, \quad \omega_L = R_A^L\omega_A + \begin{pmatrix} 0 \\ 0 \\ \dot{\nu}_2 \end{pmatrix}, \quad \omega_E = R_L^E\,\omega_L + \begin{pmatrix} 0 \\ \dot{\nu}_3 \\ 0 \end{pmatrix}. \tag{2}$$

In (2) $\dot{\nu}_1$, $\dot{\nu}_2$ and $\dot{\nu}_3$ denote rotational speeds of azimuth, x-level, and elevation control axes (z_a, z_l, y_e), respectively, as measured by resolvers/encoders.

Coordinate transformation/rotation matrices are

$$R_B^A = \begin{pmatrix} \cos\nu_1 & \sin\nu_1 & 0 \\ -\sin\nu_1 & \cos\nu_1 & 0 \\ 0 & 0 & 1 \end{pmatrix},$$

$$R_A^L = \begin{pmatrix} \sin\beta\cos\nu_2 & \sin\nu_2 & \cos\beta\cos\nu_2 \\ -\sin\beta\sin\nu_2 & \cos\nu_2 & -\cos\beta\sin\nu_2 \\ -\cos\beta & 0 & \sin\beta \end{pmatrix},$$

$$R_L^E = \begin{pmatrix} -\sin\nu_3 & 0 & -\cos\nu_3 \\ 0 & 1 & 0 \\ \cos\nu_3 & 0 & -\sin\nu_3 \end{pmatrix},$$

where β is the fixed tilt between x_a and $-z_l$.

Rotational dynamics in the elevation, x-level, and azimuth frames are

$$\sum T_E = \dot{H}_E + \omega_E \times H_E, \tag{3a}$$

$$\sum T_L = \dot{H}_L + \omega_L \times H_L, \tag{3b}$$

$$\sum T_A = \dot{H}_A + \omega_A \times H_A, \tag{3c}$$

where $\sum T$ denotes the total net torque acting on a gimbal axis, ω is the angular velocity, H is the angular momentum, and $\dot{H}$ is the local time derivative of angular momentum.

Local angular momentum vectors in mass balanced gimbals of three reference frames are

$$H_e = \mathrm{diag}(J_{ex}, J_{ey}, J_{ez})\,\omega_E, \quad H_l = \mathrm{diag}(J_{lx}, J_{ly}, J_{lz})\,\omega_L, \quad H_a = \mathrm{diag}(J_{ax}, J_{ay}, J_{az})\,\omega_A. \tag{4}$$

The total momenta in x-level and azimuth frames are

$$H_L = H_l + (R_L^E)^{\top}H_e, \quad H_A = H_a + (R_A^L)^{\top}H_L. \tag{5}$$

Substituting the kinematics and inertia relations yields (about the controlled axes)

$$T_{ey} = J_{Ey}\,\dot{q}_e - T_{de}, \quad T_{lz} = J_{Lz}\,\dot{r}_l - T_{dl}, \quad T_{az} = J_{Az}\,\dot{r}_a - T_{da}. \tag{6}$$

Total inertia of y_e, z_l and z_a axes in Equation (6) are

$$J_{Ey} = J_{ey}, \tag{7a}$$

$$J_{Lz} = J_{lz} + c^2\nu_3 J_{ex} + s^2\nu_3 J_{ez}, \tag{7b}$$

$$J_{Az} = J_{az} + c^2\nu_2\, c^2\beta(J_{lx} + s^2\nu_3 J_{ex} + c^2\nu_3)J_{ez} + 2c\nu_2 s\nu_3 c\nu_3 s\beta c\beta(J_{ex} - J_{ez}) + s^2\nu_2\, c^2\beta(J_{ly} + J_{ey}) + s^2\beta(J_{lz} + c^2\nu_3 J_{ex} + s^2\nu_3 J_{ez}). \tag{7c}$$

The disturbance torques T_{de}, T_{dl}, T_{da} are induced by hull motion.

3. Controller synthesis and robustness analysis

The control schematic for a single-axis antenna pedestal shaft is shown in Figure 3. We investigate the robust stability and performance of the azimuth-axis control system, while the design and robustness analyses for the cross-level (x-level) and elevation axes are similar. At operating points away from the singularity, elevation and azimuth servomotors compensate for changes in ship body orientation. The control objective of the elevation axis is to maintain the total angular velocity $q_e = 0$ by rotating the elevation servomotor in opposition to the ship's motion about the y_e axis. Similarly control objective of azimuth axis is to maintain the total angular velocity $r_e = 0$ by rotating the azimuth servomotor to counteract the ship's motion about the z_e axis.

3.1. Control design diagram and uncertainty specifications

Block diagram for controller design is shown in Figure 4. Nominal dynamics of forward-path elements (actuator G_a, plant G_p, sensor G_s) are

$$G_a = G_{\mathrm{amp}}\,G_{\mathrm{gm}} = \frac{K_a}{\tau_a s + 1}\cdot\frac{nK_t}{L_m s + R_m}, \quad G_p = \frac{1}{J_n}, \quad G_s = \frac{K_g\omega_g^2}{s^2 + 2\zeta_g\omega_g s + \omega_g^2}.$$

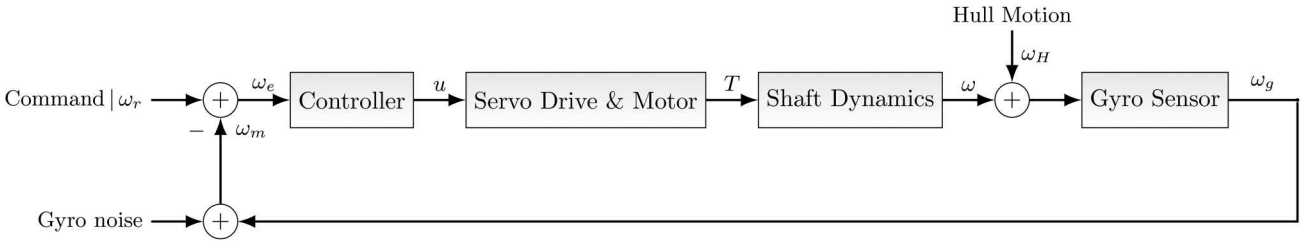

Figure 3. Control schematic for a single antenna pedestal shaft.

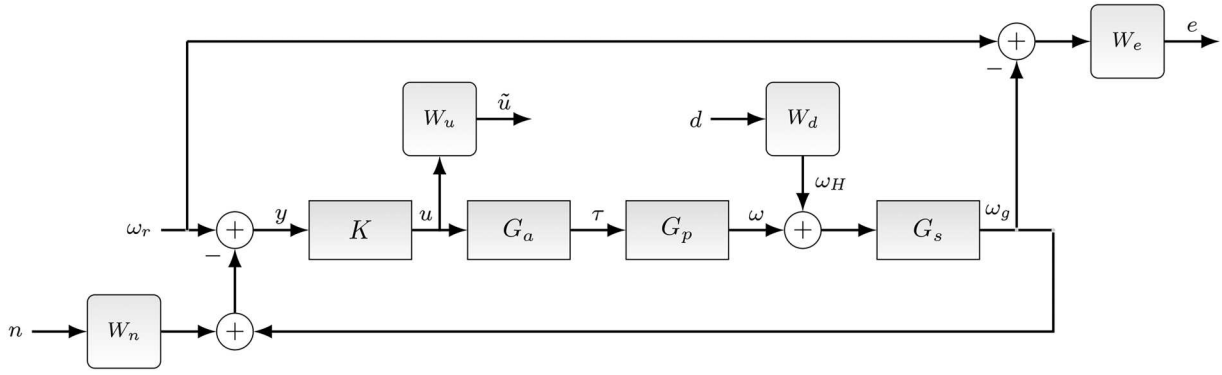

Figure 4. Block diagram of the feedback control system.

where the actuator G_a is comprised of the serial transfer functions of the power amplifier G_{amp}, and the geared servomotor G_{gm}. Back EMF is neglected. Parameters in these equations are the gain of the amplifier K_a, time constant of the amplifier τ_a, torque constant of the motor K_t, inductance of the motor coils L_m, resistance of the motor coils R_m, and the gear ratio n. Parameter in the plant transfer function G_p is J_n which denotes the average value of the azimuth axis inertia in the Equation (7c). Parameters in the sensor transfer function G_s are the gain K_g, natural frequency ω_g, and the damping ratio ζ_g of the gyro sensor.

Weights shape exogenous inputs and performance.

$$W_d = \frac{H_{\max}(\omega)\cdot s/2.2}{(s/2.2)^2 + s/2.57 + 1}, \quad W_n = \frac{0.02\cdot 200\pi}{s + 200\pi},$$
$$W_e = \frac{s/5 + 7}{s + 0.14}, \quad W_u = \frac{s/5 + 1}{0.1s/5 + 1}.$$

W_d is a band-pass filter between 0.2 and 0.5 Hz, which is the usual frequency range of the waves. W_n reflects the frequency range of the noise expected from a typical gyro sensor. W_e is a lag filter that heavily penalizes low frequency error, and rolls off at -20 dB/dec between 0.14 and 35 rad/s. W_u is a lead filter that penalizes high frequency control effort with 20 dB rise between 5 and 50 rad/s and flat afterwards.

Regarding the effect of the wave disturbance to hull motion, controller only 'sees' the angular velocity of the antenna pedestal base (which is rigidly connected to the hull) through the gyro sensor. As such it is possible to compress all the complicated physics (heading, sea state, inertia distribution, hydro damping, etc.) into a frequency-dependent gain from wave angular velocity ω_d to hull angular velocity ω_H. Hence the relation is

$$\omega_H(j\omega, \alpha) = H(j\omega, \alpha)\omega_d(j\omega).$$

Here α is wave heading relative to the axis of interest. Maximum wave angular velocity amplitude that can be expected in the wave frequency band is 1 rad/s and that sets the wave input scale. We seldom know $H(j\omega, \alpha)$ exactly, but for robust control we just need bounds across all α and inertia variations. Therefore we assume that

$$H_{\min}(\omega) \le |H(j\omega, \alpha)| \le H_{\max}(\omega), \quad \forall\ \alpha.$$

In this study, the $H_{\max}(\omega)$ term in the disturbance weighting function W_d is fixed at 1.25 for all ω.

Uncertainties in the actuator and the plant are shown in Figure 5. Backlash in the gear is represented by a multiplicative uncertainty at the output of the actuator block diagram. Azimuth axis dynamics have three uncertainties. There are two additive uncertainties: one parametric (inertia variation) and the other dynamic (friction). Third uncertainty in the azimuth axis block diagram is the dynamic multiplicative uncertainty which represents torsional flexibility of the azimuth shaft axis. To model the backlash uncertainty in the torque path, we use a

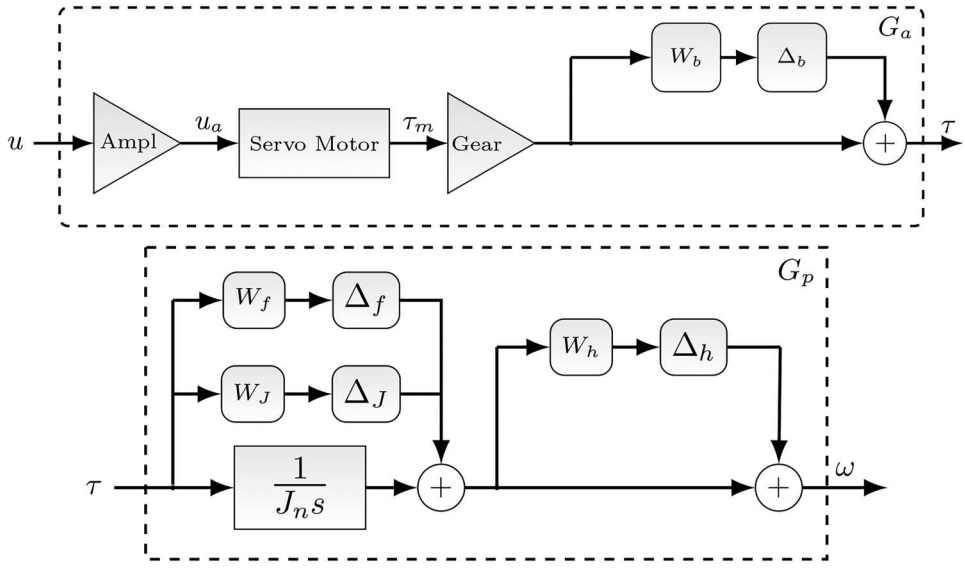

Figure 5. Uncertain actuator (top) and azimuth-axis (bottom) blocks.

weighting filter with two-plateau shape: small DC level (engagement/lost motion/back EMF) and a larger high-frequency plateau for unmodeled gear/sensor dynamics. A suitable weight for our purposes is $W_b = (0.7(s/20) + 0.11)/((s/20) + 1)$.

Variable inertia as 'seen' by the azimuth axis actuator is mainly due to the change of pitch angle of the elevation axis during stabilization. Choosing a weighting function

$$W_J = \max_{J_\delta \in (J_{\min}, J_{\max})} \left| \frac{J_n - J_\delta}{J_n J_\delta} \right| \cdot \frac{1}{s}, \quad \text{and let}$$

$$\Delta_J = \frac{J_n - J_\delta}{J_n J_\delta} \cdot \left(\max_{J_\delta} \left| \frac{J_n - J_\delta}{J_n J_\delta} \right| \right)^{-1} \Rightarrow |\Delta_J| < 1.$$

Hence weighting function for additive uncertainty on the variation of inertia is $W_J = 0.067/s$.

Static and kinetic friction can be combined as a single additive uncertainty using a non-linear weighting function such as $W_f = \max(F_{\text{max-static}}, F_{\text{max-kinetic}})$. To fit a linear weight we assign a non-zero DC gain equal to worst case static friction normalized by the actuator torque scale K_t, with a slight roll-off about stick-slip/bristle frequency. Weight chosen is $W_f = 0.2(s/0.5 + 1)/(s/2 + 1)$. This matches the friction characteristics: large at low speed (static/Coulomb), tapering as velocity increases (kinetic).

To model the torsional flexible/structural uncertainty of the azimuth axis during stabilization we use the weighting function formulation $W_h = k\,s/(s^2 + 2\zeta_n \omega_n s + \omega_n^2)$. First torsional natural frequency of the axis is computed to be 12.3 Hz based on the nominal position of antenna dish. Considering the effect of uncertainty on azimuth axis inertia, damping ratio at the natural frequency is chosen higher than normally expected material damping to amplify the angular velocity output signal components throughout the extended natural frequency range 10–15 Hz. Hence the weight used is $W_h = 1.5s/(s^2 + 46.2s + 5973)$.

3.2. Generalized plant and H_∞ control

The open-loop interconnection shown in Figure 6 admits the following input–output representation:

$$\begin{pmatrix} z_\Delta \\ z \\ y \end{pmatrix} = \begin{pmatrix} P_{11} & P_{12} & P_{13} \\ P_{21} & P_{22} & P_{23} \\ P_{31} & P_{32} & P_{33} \end{pmatrix} \begin{pmatrix} w_\Delta \\ w \\ u \end{pmatrix}, \quad w_\Delta = \Delta z_\Delta.$$

Transfer matrices in generalized plant P are partitioned to keep the structured-uncertainty channel ($w_\Delta \to z_\Delta$), the exogenous-input/performance channel ($w \to z$), and the measurement/control channel ($u \to y$) separable. The inputs are grouped as $w_\Delta = (w_b, w_J, w_f, w_h)^\top$ (the four uncertainty-channel

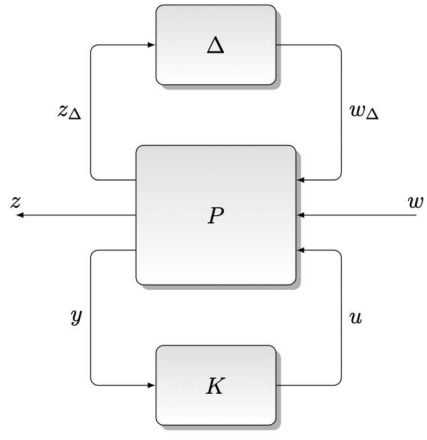

Figure 6. Generalized plant and open-loop interconnection.

inputs corresponding respectively to backlash, inertia variation, friction, and torsional flexibility), $w = (\omega_r, d, n)^\top$ (reference, wave disturbance, sensor noise), and u (the actuator command). The outputs are grouped as $z_\Delta = (z_b, z_J, z_f, z_h)^\top$ (uncertainty-channel weighted outputs), $z = (e, \widetilde{u})^\top$ (weighted performance error and weighted control effort), and y (the gyro-sensor measurement available to the controller). With this grouping, the rows of each block correspond to outputs and the columns to inputs in the same order. Block P_{11} collects the uncertainty-loop self-couplings (e.g. how the structural-flexibility block sees its own injected signal, mediated by the plant), P_{13} how the actuator forces propagate into the uncertainty outputs, P_{21} how each uncertainty input contributes to the weighted error, P_{22} how the exogenous reference/disturbance/noise are weighted into performance, P_{23} how the control effort is propagated into the weighted performance, P_{31} how each uncertainty input is felt at the measured output, P_{32} how exogenous signals reach the measurement (with the sign convention placing the disturbance and noise as negative entries because the controller sees the closed-loop angular-velocity error), and P_{33} the plant-actuator-sensor transfer from control input to measurement. Empty entries (e.g. $P_{12} = 0_{4\times3}$) reflect that the exogenous-input channel does not directly excite the uncertainty outputs in this formulation; the only coupling is through the plant, which is already captured in P_{11} and P_{13}.

$$P_{11} = \begin{pmatrix} 0 & 0 & 0 & 0 \\ W_p & 0 & 0 & 0 \\ W_f & 0 & 0 & 0 \\ W_h G_p & W_h & W_h & 0 \end{pmatrix}, \quad P_{12} = 0_{4x3},$$

$$P_{13} = \begin{pmatrix} W_b G_a \\ W_p G_a \\ W_f G_a \\ W_n G_p G_a \end{pmatrix},$$

$$P_{21} = \begin{pmatrix} W_e G_p & W_e & W_e & W_e \\ 0 & 0 & 0 & 0 \end{pmatrix},$$

$$P_{22} = \begin{pmatrix} W_e & -W_e G_s W_d & 0 \\ 0 & 0 & 0 \end{pmatrix},$$

$$P_{23} = \begin{pmatrix} W_e G_s G_p G_a \\ W_u \end{pmatrix},$$

$$P_{31} = \begin{pmatrix} -G_s G_p & -G_s & -G_s & -G_s \end{pmatrix},$$

$$P_{32} = \begin{pmatrix} 1 & -G_s W_d & -W_n \end{pmatrix}, \quad P_{33} = \begin{pmatrix} -G_s G_p G_a \end{pmatrix}.$$

Nominal closed-loop system is given by the so-called lower linear fractional transformation of the nominal part of the generalized plant $P_n := P_{2:3,2:3}$ with the controller K.

$$z = (P_{22} + P_{23}K(I - P_{33}K)^{-1}P_{32})w =: (P_n \star K)w, \tag{8}$$

Here $\star$ denotes the star product. Note that the invertibility of $(I - P_{33}K)$ is guaranteed if and only if $(I - P_{33}(\infty)K(\infty))$ is invertible. P_{33} of the generalized plant is strictly proper hence the requirement is satisfied. Our control objective is to minimize the angular velocity error of the azimuth control axis with moderate control effort, minimizing the H_∞ norm of the closed-loop system in (8). That is

$$\|P_n \star K\|_\infty : = \sup_{\omega\in\mathbb{R}} \bar{\sigma}([P_{22} + P_{23}K(I - P_{33}K)^{-1}P_{32}](j\omega)),$$

where $\bar{\sigma}$ denotes the maximum singular value.

3.3. Robust stability and performance

Incorporating the controller obtained for the nominal system from an H_∞ optimization code or using any other desired controller, the controlled interconnection of the system with the full generalized plant can be constructed. Now we have $N = P \star K$, i.e.

$$N = \begin{pmatrix} P_{11} & P_{12} \\ P_{21} & P_{22} \end{pmatrix} + \begin{pmatrix} P_{13} \\ P_{23} \end{pmatrix} K(I - P_{33}K)^{-1} \begin{pmatrix} P_{31} & P_{32} \end{pmatrix}.$$

n system in Figure 7 is then

$$z = (\Delta \star (P \star K))w = (N_{22} + N_{21}\Delta(I - M\Delta)^{-1}N_{12})w. \tag{9}$$

Note that the uncertainty block $\Delta \in RH_\infty^{4x4}$ in (9) is

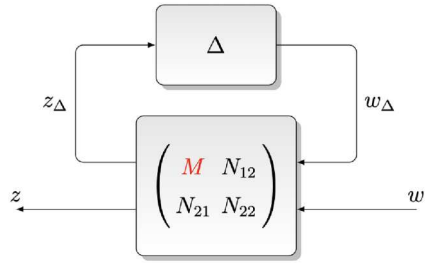

Figure 7. Controlled interconnection with structured uncertainty Δ.

structured and bounded, i.e.

$$\Delta(s) = \begin{pmatrix} \delta_b(s) & 0 & 0 & 0 \\ 0 & \delta_J & 0 & 0 \\ 0 & 0 & \delta_f(s) & 0 \\ 0 & 0 & 0 & \delta_h(s) \end{pmatrix}, \quad \text{and}$$

$$\|\delta_b(s)\|_\infty,\ |\delta_J|,\ \|\delta_f(s)\|_\infty,\ \|\delta_h(s)\|_\infty \text{ are all } < 1.$$

Bounded diagonal blocks is equivalent to $\|\Delta\|_\infty < 1$.

The uncertain closed-loop system (9) is stable if and only if $(I - M\Delta)$ is invertible for all possible values of Δ within the set $\{\mathbf{\Delta} : \|\mathbf{\Delta}\|_\infty < 1\}$. Consequently, we define the structured singular value

$$\mu_{\mathbf{\Delta}}(M) := \frac{1}{\inf_{\mathbf{\Delta}}\{\bar{\sigma}(\Delta) : \det(I - M(jw)\Delta) = 0\}}. \quad (10)$$

Robust stability is guaranteed if $\mu_{\mathbf{\Delta}}(M) < 1$. Hence, robust stability of nominally stable $N(j\omega)$ is achieved if and only if $\mu_{\mathbf{\Delta}}(M(j\omega)) < 1$ for all $\omega \in \mathbb{R} \cup \infty$.

Before instability occurs, closed-loop performance often degrades to an unacceptable level. Therefore, it is necessary to test the performance of the robustly stable plant under disturbances, which reveals the worst-case degradation for a given level of perturbation. Nominally stable uncertain linear system $N(j\omega)$ with nominal performance $\|N_{22}\|_\infty < \gamma$ can achieve a robust performance if it is robustly stable and $\|\Delta \bigstar N\|_\infty = \|N_{22} + N_{21}\Delta(I - M\Delta)^{-1}N_{12}\|_\infty < 1$ for all possible values of Δ within the set $\{\mathbf{\Delta} : \|\mathbf{\Delta}\|_\infty < 1\}$. This condition is equivalent to $\mu_{\mathbf{\Delta}_e}(N) < 1$, with $\mathbf{\Delta}_e := diag(\mathbf{\Delta}\, \mathbf{\Delta}_f)$, such that $\mathbf{\Delta}_e \in \mathbb{C}^{n_{(w_\Delta + w)} \times n_{(z_\Delta + z)}}$. Here we incorporate an additional fictitious uncertainty block Δ_f in the set $\{\mathbf{\Delta}_f : \|\mathbf{\Delta}_f\|_\infty < 1\}$.

4. Numerical simulations and results

Numerical values for a representative system is given in Table 1 (Kuseyri 2017a). To benchmark the H_∞ design against a fair, well-tuned classical baseline, a PI controller $K_{\mathrm{PI}}(s) = k_p + k_i/s$ is designed for the same nominal plant $G(s) = G_s(s)\, G_p(s)\, G_a(s)$ used in the H_∞ synthesis. The tuning targets the same disturbance band 0.2–0.5 Hz (i.e. 1.26–3.14 rad/s) so that the comparison reflects controller architecture rather than bandwidth selection. With the sensitivity function $S(j\omega) = 1/(1 + L(j\omega))$ where $L = K_{\mathrm{PI}}G$, in-band disturbance rejection $|S(j\omega)| \ll 1$ requires $|L(j\omega)| \gg 1$, which sets the integral gain. Selecting an open-loop crossover frequency $\omega_c \approx 7$ rad/s places the disturbance band roughly a decade below crossover (so $|S| \lesssim -15$ dB in-band) while keeping ω_c at least a decade below the gyro corner $\omega_g = 614$ rad/s and the first torsional mode at 77.3 rad/s (12.3 Hz), so that the noise weight W_n, the flexibility weight W_h, and the sensor dynamics G_s do not amplify roll-off content. The proportional gain is then chosen to provide a phase margin of approximately 60° at ω_c, which corresponds to $k_p \approx 1/|G(j\omega_c)|$, and the integral gain is set to $k_i = k_p\, \omega_i$ with $\omega_i \approx \omega_c/3 \approx 2.3$ rad/s so that the integrator does not erode the phase margin. The resulting controller is $K_{\mathrm{PI}}(s) = k_p(1 + \omega_i/s)$ with numerical values $k_p = 8.1$ and $k_i = 18.6$, giving an open-loop gain $|L(j\omega)| \approx 25$ dB at 0.35 Hz (the center of the disturbance band) and a gain margin in excess of 12 dB. No structure preceding this controller (no inner torque loop, no friction compensation, no anti-windup) is added, in order to keep the comparison representative of single-loop classical practice.

Table 1. Pedestal/actuator/sensor data.

Symbol	Value	Unit	Symbol	Value	Unit
J_{ex}	0.63	kg·m²	J_{lz}	0.40	kg·m²
J_{ey}	0.69	kg·m²	J_{ax}	3.07	kg·m²
J_{ez}	0.86	kg·m²	J_{ay}	4.13	kg·m²
J_{lx}	0.53	kg·m²	J_{az}	2.61	kg·m²
J_{ly}	0.15	kg·m²	R_m	1.22	Ω
K_g	5.7	V/V	ζ_g	0.45	–
L_m	5.13	mH	K_t	0.21	N·m/A
K_a	3500	V·s/V	τ_a	$3.75 \cdot 10^{-4}$	s
n	50	–	ω_g	614	rad/s

The motion of the hull under the superposition of several disturbance waves in the frequency range of 0.2–0.5 Hz, and the resulting error in the instantaneous angular velocities of the controlled systems, are shown in Figure 8. The simulation results are presented for the nominal system as well as for five randomly selected uncertain systems. H_∞ control demonstrates clear superiority over PI control, as evident in Figure 9. The plots show the frequency response of the PI- and H_∞-controlled systems from disturbance to angular frequency error, both for the nominal system and randomly selected uncertain systems. It can be clearly seen that in the 0.2–0.5 Hz band, the H_∞-controlled systems (red dashed lines) provide at least 10 dB greater disturbance attenuation than the PI-controlled systems (blue dashed lines). The step responses of the nominal system and five randomly selected uncertain systems in Figure 10 reveal analogous performance.

Computation of nominal performance, expressed as the maximum singular value of the MIMO system $G_{\mathrm{perf}} : (\omega_r, d, n)^\top \to (e, \tilde{u})^\top$, yields 0.764 with PI control and 0.453 with H_∞ control. The H_∞ controller achieves significantly better performance than the PI controller. However, μ-analysis indicates that the system's robust stability holds for at most 77% of the specified maximum uncertainty range. This result is presented in Figure 11.

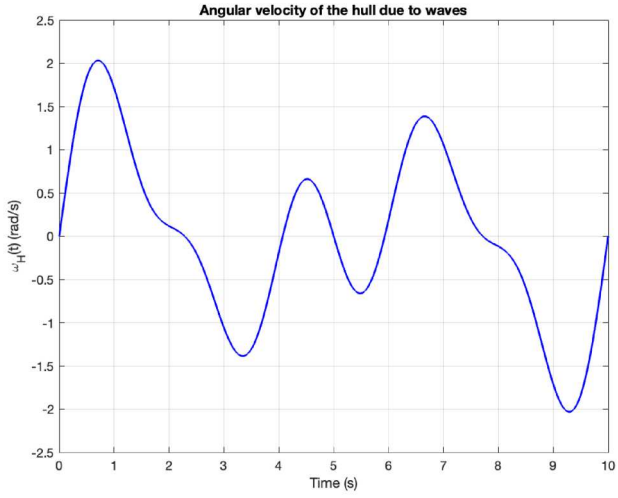

(a) Hull angular motion (multi-sine, 0.2–0.5 Hz)

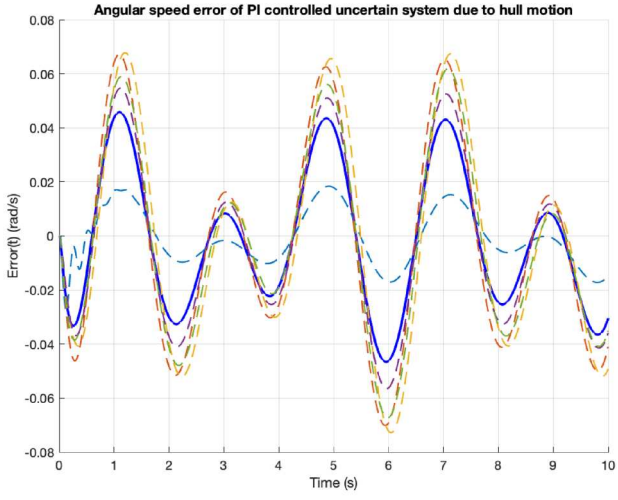

(b) Angular velocity error, PI control

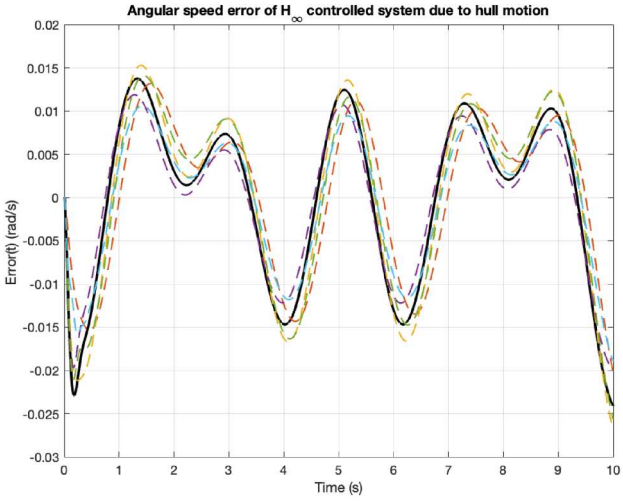

(c) Angular velocity error, H_∞ control

Figure 8. Time-domain responses for nominal and randomly sampled uncertain systems. (a) Hull angular motion (multi-sine, 0.2–0.5 Hz) (b) Angular velocity error, PI control (c) Angular velocity error, H_∞ control.

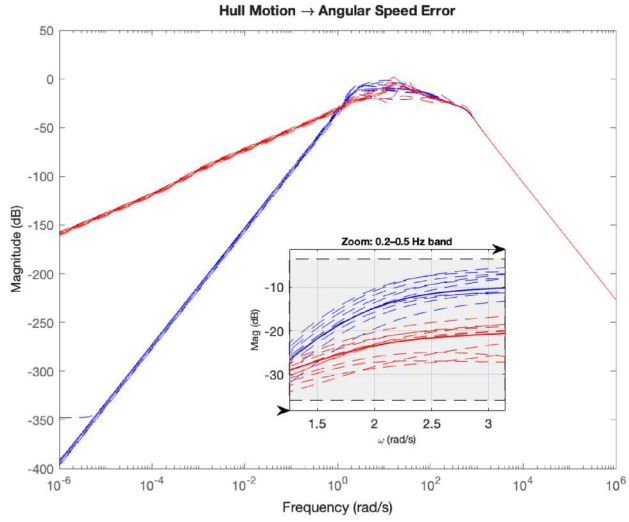

Figure 9. Disturbance to angular speed-error frequency responses (nominal and random uncertain samples).

Figure 12(a) presents the relative contributions of the four modeled uncertainties to closed-loop instability in the form of a pie chart. This distribution highlights which uncertainty sources dominate the robustness margin and therefore require closer attention in design. Furthermore, Figure 12(b) shows the effect of a 25% increase in each uncertainty on system stability, expressed as a bar chart. This analysis provides a comparative measure of sensitivity, indicating how much the stability margin deteriorates when each uncertainty grows beyond its nominal bound. The results confirm that increasing friction leads to the most significant degradation of the stability margin, while the impact of backlash remains secondary. Together, these demonstrate that the system's robustness is primarily constrained by friction and backlash, and any improvement in these areas would provide the greatest benefit.

Regarding robust performance, the μ-analysis yields values greater than one across all frequencies as shown in Figure 13, indicating that the closed-loop system fails to achieve robust performance. To identify the dominant sources of performance degradation, two complementary analyses were performed. Figure 14(a) presents the per-block influence on the weighted performance using single-block substitution, while Figure 14(b) quantifies the single-block influence at the critical frequency of 21.3 rad/s. Both figures consistently demonstrate that friction and backlash uncertainties have the most severe impact on performance, paralleling their dominant role observed in the robust

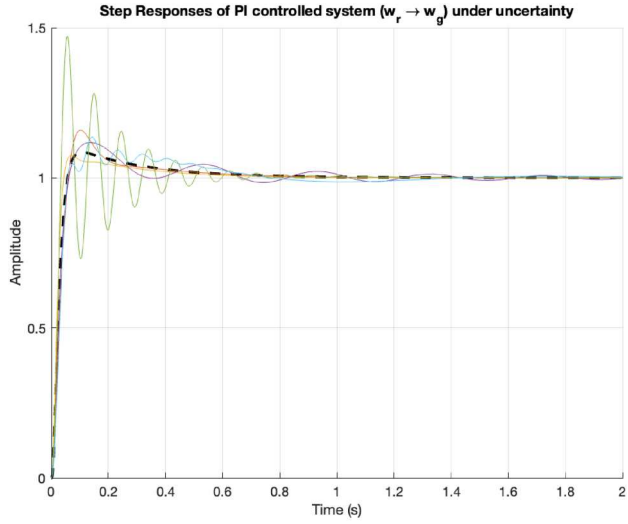

(a) PI-controlled step responses

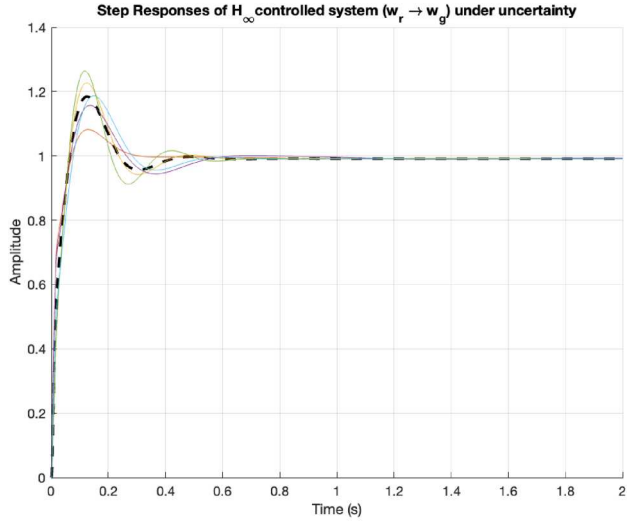

(b) H_∞-controlled step responses

Figure 10. Nominal and uncertain step responses. (a) PI-controlled step responses (b) H_∞-controlled step responses.

stability analysis. These results highlight that attenuation of friction and backlash effects is essential for enhancing the system's overall robustness.

5. Discussion and conclusion

In this paper, we investigated the robust stability and robust performance of a three-axis ship-mounted mobile antenna stabilization system. The azimuth axis was selected for detailed analysis, as it is the most affected by dynamic coupling. Typical uncertainties in the system dynamics were specified, and an H_∞ controller was synthesized for the closed-loop uncertain system. The results show that, under the defined uncertainty specifications,

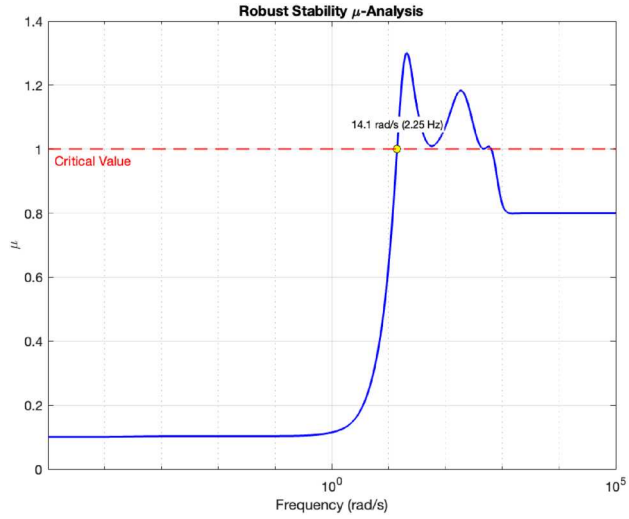

Figure 11. Robust stability μ-plot.

the system exhibits a slightly negative robust stability margin and fails to achieve robust performance. The dominant sources of stability and performance degradation were identified as friction and backlash.

The per-block μ-decomposition (Figures 12 and 14) identifies friction W_f and backlash W_b as the dominant contributors, so the candidate remedies are not equally cost-effective; a prioritized agenda follows from the decomposition. All share the objective of improving robustness near the critical frequency of 21.3 rad/s, but each carries trade-offs in control complexity, bandwidth and noise margin, and modeling/identification demands. *First*, a model-based LuGre or generalized-Maxwell-slip friction compensator estimated online (Sariyildiz et al. 2020; Wang et al. 2018; Lyu et al. 2022) reduces W_f at low and mid frequencies, where its attribution is largest, at the cost of a commissioning-time identification routine. *Second*, an inner torque loop with bidirectional torque biasing or a reference governor desensitizes the outer loop and reduces the high-frequency W_b plateau without added observer dynamics. *Third*, a μ-synthesis D-K iteration on the existing generalized plant, with W_f, W_b re-weighted for the residual uncertainty after the first two remedies, is the natural next-controller step. *Fourth*, replacement with a composite disturbance-observer + outer-loop architecture (Wang et al. 2018; Lyu et al. 2022, 2026) can dominate H_∞ when disturbance content is mostly low- and mid-frequency, as here. The remaining paths (backlash inversion or compliance in isolation, a reference governor alone, or μ-synthesis without first addressing friction) are second-order: the per-block analysis predicts they cannot recover the $\mu < 1$ margin without also reducing the friction block. Detailed synthesis and validation of each remedy is a separate study.

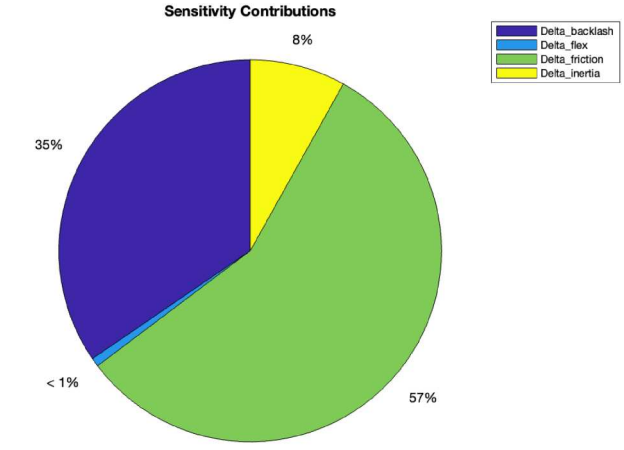

(a) Per-uncertainty contribution to instability

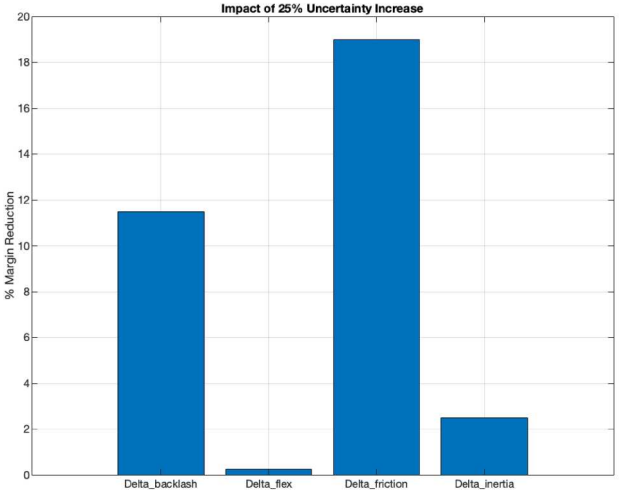

(b) Effect of uncertainty size increase per block

Figure 12. Dominant constraints on robust stability. (a) Per-uncertainty contribution to instability (b) Effect of uncertainty size increase per block.

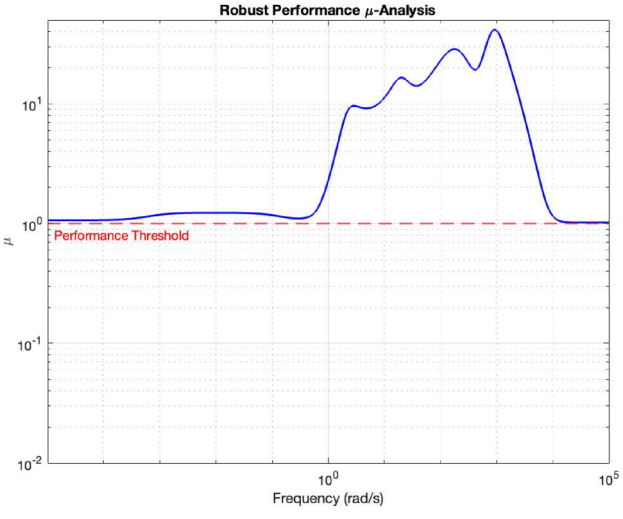

Figure 13. Robust performance μ-plot.

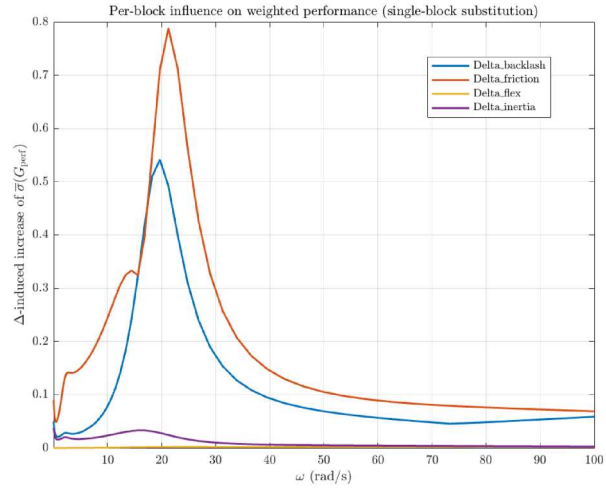

(a) Per-block influence on the weighted performance

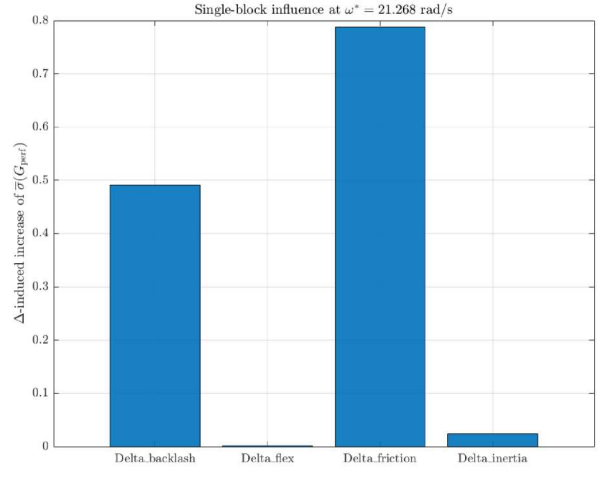

(b) Single-block influence at the critical frequency of 21.3 rad/s

Figure 14. Contributions to worst-case performance degradation. (a) Per-block influence on the weighted performance (b) Single-block influence at the critical frequency of 21.3 rad/s.

A further consideration is that μ-analysis can be conservative under multiple dynamic uncertainties, evaluating worst-case realizations frequency-by-frequency without enforcing causality or cross-frequency coupling. Integral quadratic constraints (IQCs) incorporate these properties through dynamic multipliers and can yield less conservative assessments. Future work will investigate IQC-based robust stability analysis and synthesis to reassess margins, explore controller designs with reduced conservatism, and pursue experimental validation and reduced-order controller development.

Finally, it should be noted that the present study adopts solely a numerical approach. The H_∞ synthesis, μ-analysis, and per-block decomposition are model-based procedures whose outputs depend on the analytic

specifications of the weighting filters W_b, W_J, W_f, W_h rather than on a specific hardware realization. The reported friction- and backlash-dominance conclusion is therefore a property of the model class and is robust to the specific hardware on which it is eventually deployed, provided the same uncertainty bounds apply. Nevertheless, hardware-in-the-loop validation of a specific controller, which requires a calibrated gimbal test rig instrumented for friction and backlash identification, is the natural next step in the research program outlined above.

Author contributions

CRediT: **İbrahim Sina Kuseyri:** Conceptualization, Formal analysis, Investigation, Methodology, Validation, Writing – original draft, Writing – review & editing.

Disclosure statement

The author declares no potential conflicts of interest with respect to the research, authorship, and/or publication of this article, and further declares that they have no known competing financial interests or personal relationships that could have appeared to influence the work reported in this paper.

ORCID

İbrahim Sina Kuseyri http://orcid.org/0000-0001-8134-7046

Data availability statement

The data that supports the findings of this study are openly available in Harvard Dataverse at https://doi.org/10.7910/DVN/CIT23E.

References

Baskın M, Leblebicioğlu K. 2017. Robust control for line-of-sight stabilization of a two-axis gimbal system. Turk J Electr Eng Comput Sci. 25:3839–3853. https://doi.org/10.3906/elk-1606-435

Hajjem M, Lanusse P, Victor S, Melchior P, Thomas L. 2022. Robust control of two-axis tracking antennas using CRONE approach. IFAC-PapersOnLine. 55(40):169–174. https://doi.org/10.1016/j.ifacol.2023.01.067

Hong S, Cho KD. 2012. Kinematic algorithms and robust controller design for inertially stabilized system. IEEE ASME Trans Mechatron. 9(1):76–87. https://doi.org/10.1109/TMECH.2012.2223228

Kim SB, Kim SH, Kwak YK. 2010. Robust control for a two-axis gimbaled sensor system with multivariable feedback systems. IET Control Theory Appl. 4(4):539–551. https://doi.org/10.1049/iet-cta.2008.0195

Kuseyri İS. 2017b. MIMO H_∞ control of three-axis ship-mounted mobile antenna systems. Int J Control. 91(2):1–13. https://doi.org/10.1080/00207179.2017.1279755

Kuseyri S. 2017a. Modelling and stabilization of a three-axis ship-mounted mobile antenna system. Proc Inst Mech Eng, Part M: J Eng Marit Environ. 231(2):533–541. https://doi.org/10.1177/1475090216661908

Lee DH, Tran DQ, Kim YB, Chakir S. 2020. A robust double active control system design for disturbance suppression of a two-axis gimbal system. Electronics. 9(10):1638. https://doi.org/10.3390/electronics9101638

Love LJ, Jansen JF, Pin FG. 2004. On the modeling of robots operating on ships. In: Proceedings of the IEEE International Conference on Robotics and Automation; New Orleans, LA, USA. IEEE. p. 2436–2443. https://doi.org/10.1109/ROBOT.2004.1307426

Lyu B, Liu C, Yue X, Shi L. 2026. Nonfragile super-twisting disturbance-observer-based inverse optimal control for spacecraft with integrated dynamics. IEEE Trans Aerosp Electron Syst. 62:6143–6152. https://doi.org/10.1109/TAES.2026.3662312

Lyu B, Liu X, Wei X. 2022. Constrained multi-observer-based fault-tolerant disturbance-rejection control for rigid spacecraft. Int J Robust Nonlinear Control. 32(11):6505–6521. https://doi.org/10.1002/rnc.6270

Nguyen DH, Nguyen VH. 2019. Robust control of two-axis gimbal system. In: Proceedings of the International Symposium on Electrical and Electronics Engineering; Ho Chi Minh City, Vietnam. IEEE. p. 177–182. https://doi.org/10.1109/ISEE2.2019.8921070

Ren W, Qiao Q, Nie K, Mao Y. 2019. Robust DOBC for stabilization loop of a two-axes gimbal system. IEEE Access. 7:110554–110562. https://doi.org/10.1109/ACCESS.2019.2933447

Safa A, Abdolmalaki RY. 2019. Robust output feedback tracking control for inertially stabilized platforms with matched and unmatched uncertainties. IEEE Trans Control Syst Technol. 27(1):118–131. https://doi.org/10.1109/TCST.2017.2761324

Şahin M. 2024. Stabilization of two axis gimbal system with self tuning PID control. J Polytech. 27(4):1441–1452. https://doi.org/10.2339/politeknik.1210906

Sariyildiz E, Oboe R, Ohnishi K. 2020. Disturbance observer-based robust control and its applications: 35th anniversary overview. IEEE Trans Ind Electron. 67(3):2042–2053. https://doi.org/10.1109/TIE.2019.2903752

Wang Y, Tian D, Dai M. 2018. Composite hierarchical anti-disturbance control with multisensor fusion for compact optoelectronic platforms. Sensors. 18(10):3190. https://doi.org/10.3390/s18103190